ADVANCES IN THE LONG-PULSE STEADY-STATE HIGH BETA H-MODE SCENARIO WITH ACTIVE CONTROLS OF DIVERTOR HEAT AND PARTICLE FLUXES IN EAST

B. N. Wan[1*], X. Z. Gong[1], Y. Liang[1, 2], N. Xiang[1], G. S. Xu[1], Y. Sun[1], L. Wang[1], J. P. Qian[1], H. Q. Liu[1], B. Zhang[1], T. Y. Xia[1], J. Huang[1], R. Ding[1], T. Zhang[1], G. Z. Zuo[1], Z. Sun[3], L. Zeng[1], X. J. Zhang[1], Q. Zang[1], B. Lyu[1], A.M. Garofalo[4], G. Q. Li[1], K. D. Li[1], Q. Q. Yang[1], for the EAST team** and Collaborators**

[1] Institute of Plasma Physics, Chinese Academy of Sciences, Hefei 230031, China

[2] Forschungszentrum Jülich GmbH, Institute of Energy and Climate Research -Plasma Physics (IEK-4), Association EURATOM-FZJ, 52425 Jülich, Germany

[3] Princeton Plasma Physics Laboratory, Princeton, NJ, United States of America

[4] General Atomics San Diego, California, USA

*Contact Email: bnwan@ipp.ac.cn

**_See Appendix_

Abstract

Since the last IAEA-Fusion Energy Conference, the Experimental Advanced Superconducting Tokamak (EAST) research program has been, in support of ITER and CFETR, focused on development in terms of the long-pulse steady-state (fully noninductive) high beta H-mode scenario with active controls of the stationary and transient divertor heat and particle fluxes. The operational domain of the steady-state H-mode plasma scenario has been significantly extended with ITER-like tungsten mono-block divertor, plasma control and heating schemes. EAST has achieved several important milestones in the development of high β_p H-mode scenario and its key physics and technologies. A 60 s-scale long-pulse steady-state high β_p H-mode discharge with the major normalized plasma parameters similar to the designed performance of the CFETR 1GW fusion power operation scenario has been successfully established and sustained by pure RF heating and current drive. Several feedback control schemes have been developed for a sustained detachment with good core confinement. This includes control of the total radiation power, target electron temperature, and particle flux measured using divertor Langmuir probes or a combination of the control of target electron temperature and AXUV radiation near the X point. The detachment feedback control schemes have been integrated with small-ELM regimes and high β_p scenario via neon seeding, enabling a core and edge compatible integrated high-beta scenario applicable to long-pulse operations. ELM suppression has been achieved using various methods, including resonant magnetic perturbations and impurity seeding. Full suppression of ELMs by using n=4 RMPs has been demonstrated for ITER for the first time in low input torque plasmas in EAST. EAST has been operated with helium to support the ITER research requirements for the first time. For a long-pulse, high bootstrap current fraction operation, a new lower tungsten divertor with active water-cooling has been installed, along with improvements in the heating and current drive capability.

1. INTRODUCTION

As a long-term research program for superconducting tokamaks, the Experimental Advanced Superconducting Tokamak (EAST) (major radius $R \leqslant 1.9$ m, minor radius $a \leqslant 0.45$ m, plasma current $Ip \leqslant 1$MA, and toroidal magnetic field $B_T \leqslant 3.5$T) aims to provide a suitable platform to address the physics- and technology-related issues relevant to steady-state advanced high-performance H-mode plasmas with ITER-like configuration, plasma control and heating schemes [1]. To reach this goal, EAST has been equipped with lower hybrid current drive (LHCD) systems (2.45 GHz (4 MW)/4.6 GHz (6 MW) klystron power), an electron cyclotron heating (ECH) system (140 GHz (2 MW) gyrotron power), an ion cyclotron resonant frequency (ICRF) system (27 MHz–80 MHz (12 MW) generator power), and balanced neutral beam injection (NBI) systems (two co-current and two counter-current NBI sources; 80 keV/4 MW). In the past few years, EAST has been upgraded with an ITER-like active water-cooling tungsten divertor that can handle a power load of up to 10 $MW \cdot m^{-2}$ for long-pulse steady-state operations with high power injection. Therefore, the experience and understanding of the high-performance long-pulse operation in EAST will be valuable for the development of future fusion devices, namely ITER and CFETR [2, 3].

This paper presents the recent experimental results of EAST obtained since the 27th IAEA Fusion Energy Conference (FEC) in 2018, with emphasis on the highly normalized poloidal beta (β_p) scenario development and key physics related to the advanced high-performance steady-state H-mode plasmas. The recent achievements in the long-pulse operation and extension of the operational regime are discussed in Section 2. Section 3 presents the progress made in terms of advances in active controls of divertor heat and particle fluxes in support of steady state operation. The physics progress in support of ITER is shown in Section 4. Future plans for the EAST program are described in Section 5.

2. ADVANCES IN THE LONG-PULSE STEADY-STATE HIGH BETA H-MODE SCENARIO

The demonstration of a high-performance steady-state H-mode operation with a reactor-like metal wall, a low momentum input, and electron dominated heating scheme is a critical step towards the success of economical fusion energy. In EAST, several key technical challenges related to the development of high-performance steady-state H-mode operation, have been investigated. A series of important breakthroughs in frontier physical topics including active controls of divertor heat and particle fluxes, and mitigation of transient heat load associated with edge-localized-modes (ELMs), are addressed.

A discharge for a duration of over 60 s with $\beta_p \sim 2.0$, normalized beta $\beta_N \sim 1.6$, confinement improvement factor $H_{98y2} \sim 1.3$ and internal transport barrier on the electron temperature profile has

been obtained by multi-RF power heating and current drive of ~2.5 MW LHW and 0.9 MW ECH, shown in figure 1, with an upper single null (USN) plasma configuration with strike points on the tungsten divertor [4]. The loop voltage was well controlled to ~ 0, indicating the fully noninductive current drive condition. Small ELMs (f_{ELM} ~ 100-200 Hz) were maintained in this long pulse H-mode discharge. To achieve such a long pulse operation, the optimization of the X-point position, the outer gap, and local gas puffing near the LHW antenna were investigated to maintain RF power coupling and avoid hot-spot formation on the 4.6 GHz LHW antenna. The global parameters of B_T ~ 2.4T and line-averaged electron density n_e ~ 3.5×10^{19} m^{-3} were optimized for high current drive efficiency of the LHW and on-axis deposition of the ECH. The on-axis ECH was applied not only to the core electron heating, but also to eliminate accumulation of high Z_{eff} impurities in the core plasmas. Notably, the long-pulse discharge presented here is controlled shutdown. But still several difficulties, particularly the strong hot spot on the lower divertor and particle recycling, have been encountered in the development of these long-pulse H-mode discharges and limits further extension of plasma pulse duration [5].

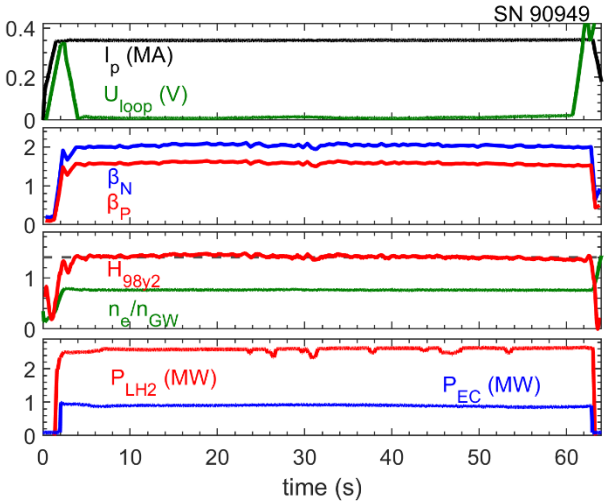

FIG. 1 Time histories of several parameters for EAST 60 s high-β_p long-pulse discharge in EAST. From top to bottom: plasma current, loop voltage, normalized poloidal beta, normalized beta, confinement improvement factor H_{98y2}, the density normalized to Greenwald density n_e/n_{GW}, and RF heating power of LHW and ECH.

An internal transport barrier (ITB) near ρ ~ 0.3 was formed in electron temperature with T_{e0} ~ 5.6 keV, accounting for the improved confinement quality. The current density profiles are calculated based on the analysing of the ONETWO transport code after the equilibrium reconstruction process, where the electron cyclotron current drive (ECCD) is obtained from the TORAY code; the LHCD is obtained using the GENRAY and CQL3D code; and the bootstrap current is calculated using the Sauter model [6]. A monotonic q profile is obtained and no sawtooth activities were observed during the whole discharge which is consistent with the measured q profile, where the minimum q, q_{min}, is

above 1. Notably, the bootstrap-current fraction (f_{bs}) is nearly 50% with β_p up to 2.0 in this long-pulse discharge, and the LHCD and ECCD contributes 42% and 8% of the plasma current, respectively.

More experimental studies were performed on the high β_p scenario with high f_{bs}. EAST experiments have shown improved confinement and reduced turbulence when plasma operation regimes were extended to higher β_p [7]. A higher β_p with a high energy confinement was observed at a high density, consistent with previous observations on JT-60U [8] and DIII-D [9] with dominated ion heating. An important feature of such a high-β_P H-mode plasma scenario is that, mainly because of the stabilization effect of the Shafranov shift on the plasma turbulence, higher β_P results in better plasma confinement. In EAST, electron heating is predominantly with the equipped heating and current drive systems. In this high β_P H-mode plasma scenario, the electron turbulent energy fluxes decrease with the increase in β_p, whereas the ion turbulent energy flux is low and decreases gradually with the increase in β_P. The high electron energy flux due to the electron heating by RF power ($T_e >> T_i$) and the transport are dominantly governed by the trapped electron mode (TEM) in EAST, discussed in details in reference [7].

Moreover, a clear positive dependence of H_{98y2} on the density peaking factor was found in such high β_P H-mode plasma scenarios [10]. Four categories of discharges with nearly same β_P in each category but different heating combinations, namely LH only, LH+EC, LH+NB and LH+EC+NB, were compared to exclude contribution to confinement improvement from Shafranov shift and external torque injection. Figure 2 shows a scatter plot of the confinement improvement factor H_{98y2} against the density peaking factor from the four categories of discharges. An increase in H_{98y2} is significant in all the four cases, by 20%–30% within the range of achievable density peaking factor in the experiments. In particular, for the case of LH+EC discharges, a remarkable increase of H_{98y2} from 1.0 to > 1.3 has been obtained, as shown in Fig. 2, with the density peaking factor increasing from ~1.4 to ~1.7 at a fixed β_p. A further simulation suggested that a high-density gradient promotes the ITB formation in high β_p plasmas [7]. This category of discharge is more reactor relevant as it is heated by pure RF powers which predominantly heats electrons with nearly zero external torque injection as projected for the burning plasma, which might further benefit the development of the high-β_p plasma scenario toward a high-density regime.

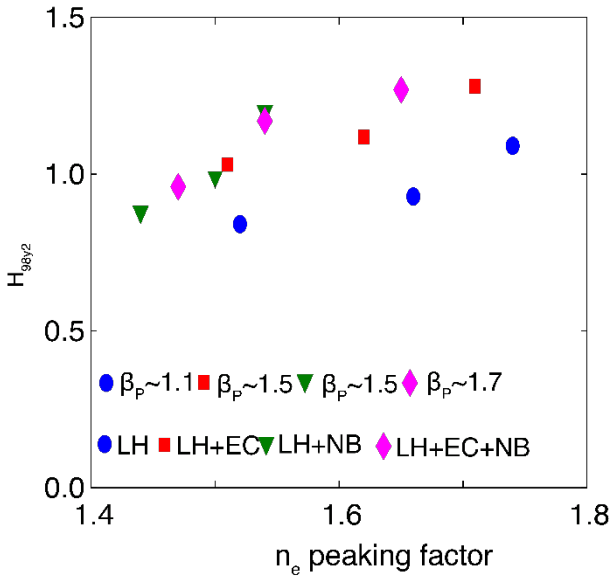

FIG. 2 Energy confinement improvement factor H_{98y2} versus density peaking factor n_e for four categories of discharges in EAST.

To extend the high β_p plasma scenario towards a higher beta and higher f_{bs} regime, NBI is added in the high-β_p scenarios of the RF-only target H-mode discharges, in the medium density range (3.0-4.0×10^{19} m^{-3}). Although plasmas with RF heating in combination with NBI have higher $\beta_p \sim 2.0$ compared with target long-pulse RF-only H-mode discharges with $\beta_p \sim 1.2$, f_{bs} is ≤ 30% in both the cases. A TRANSP analysis shows that this is mostly because the fast ions in the NBI plasmas increase β_p but do not contribute significantly to the neoclassical bootstrap current [11]. Thus, to demonstrate improved high-β_p performance with high f_{bs}, fast-ion confinement is further optimized in EAST. The key parameters (plasma current, electron density and beam energy) have been simultaneously scanned in experiments to study the fast-ion characteristics of each beam line in conjunction with reducing the fast-ion loss. The experimental results show that the prompt loss from counter-injection beams is significant; nevertheless, it can be reduced by decreasing the beam voltage, and the shine-through loss can be decreased at a higher density and lower beam voltage, consistent with simulations. Recently, at a higher density (4.7×10^{19} m^{-3}, $f_{GW} \sim$ 0.6-0.8) under an optimized beam voltage, fully noninductive high-β_p scenarios with a total power of 2.7MW LHW, 1.0MW ECH and 2.4MW NBI were significantly extended to improve plasma performance ($\beta_p \sim 2.5$, $\beta_N \sim 2.0$ and $H_{98y2} > 1.1$) with $f_{bs} \sim$ 50%, as shown in Fig. 3. The analysis showed the fast-ion contribution to the total plasma energy and the effects on confinement in this high-β fully noninductive plasma. The fast-ion pressure significantly decreased with respect to the total pressure, which is one of the important factors to increase the bootstrap current [12]. Besides, the fast-ion pressure and density, as well as the current carried by the fast ions, can now be directly measured in EAST [13]. Velocity-space tomography based on FIDA measurements in at least two lines of view can be applied to measure the fast-ion velocity distribution functions [14]. The zeroth moment gives the fast-ion density, the first moment

the fast-ion current, and the second moment the fast-ion pressure [15]. These new measurements in EAST allow a direct comparison of the fast-ion measurements with TRANSP simulations and provide a useful guidance for optimization of high β_p scenarios with NBI. FIDA measurements were combined with neutron emission spectroscopy measurements for the first time which now allow these measurements for all ion energies [13].

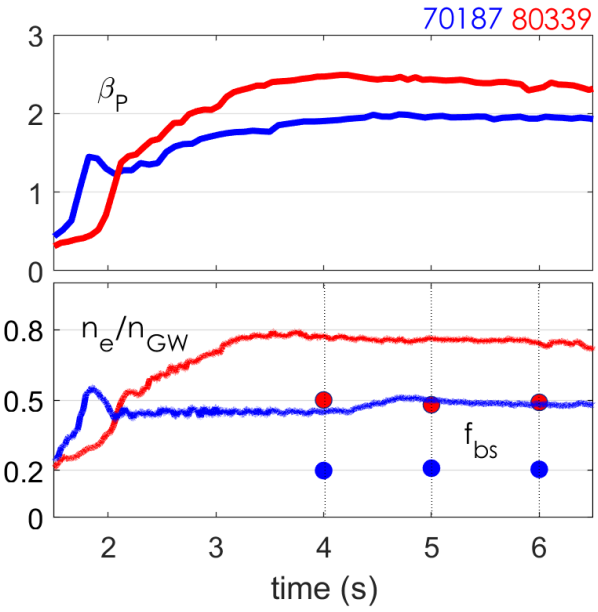

FIG. 3 Time traces of two high β_p discharges with NBI heating in EAST. From top to bottom, normalized poloidal beta, the density normalized to Greenwald density n_e/n_{GW}, and bootstrap current fraction.

To demonstrate such a β_p scenario for long pulse operation, the neutral beam injection systems were operated in modulated mode using two ion sources with duty time of 50% for each. A higher β_N ~1.8 with a duration of 20 s is achieved using the co-current modulated neutral beam (shown in figure 4). The high-Z impurity accumulation in the plasma core was well controlled at a low level using the on-axis ECH and by reducing the fast ion losses through beam energy optimization. Other features, such as the metal wall (tungsten divertor), low torque injection (T_{inj} ~ 1.0 N·m), electron-dominated heating ($T_e > T_i$), moderate bootstrap current fraction (f_{bs} ~ 50%), broadened current density profile with the central q(0) > 1.0 and good energy confinement, have also been demonstrated in this scenario. These plasma regimes satisfy the research goal of the highly integrated performance. Several normalized parameters β_p ~ 2.0, β_N ~ 1.8, H_{98y2} ~ 1.3, and n_e/n_{GW} ~ 0.75 are close or even higher than the designed performance for 1 GW scenario of the CFETR steady-state, as shown in figure 5.

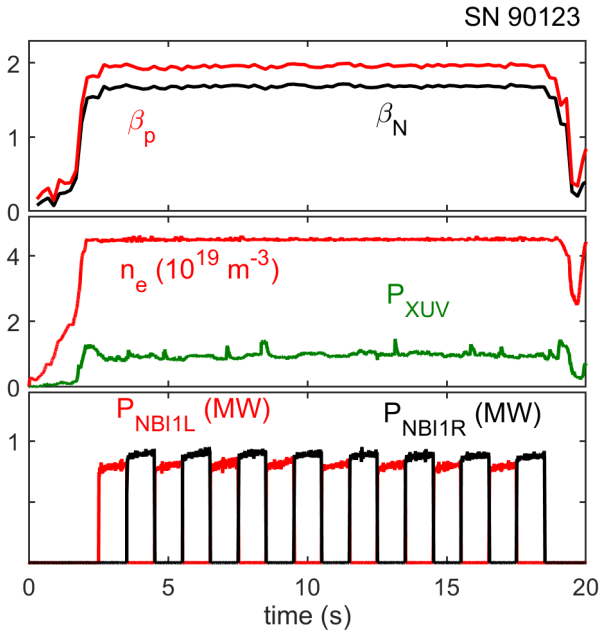

FIG. 4 From top to bottom: time traces of β_p and β_N, line average density and current in one PF coil, XUV signal, injected power of modulated NBI for EAST 20 s long-pulse high-β_p discharge #90123.

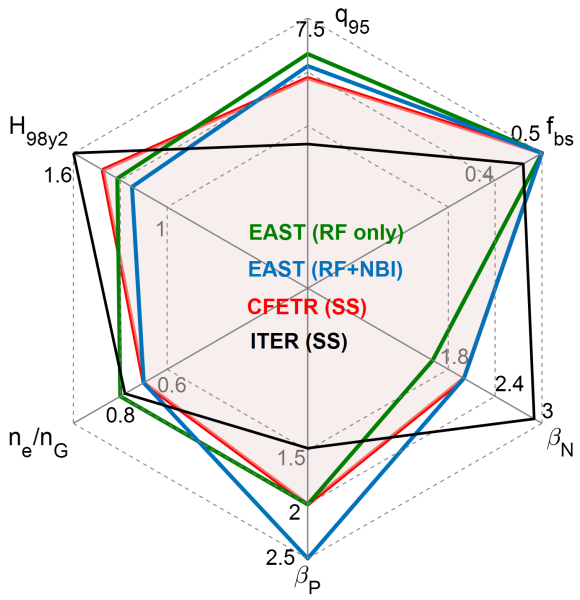

FIG. 5 Integrated plasma performance in EAST (RF only), EAST (RF + NBI), ITER (SS) and CFETR (SS).

Control of heat flux on the divertor plates is essential for higher power injection to achieve long pulse high β plasma operation. More recently, EAST has successfully demonstrated a compatible core and edge integration in high β_p scenarios via feedback control of the total radiation power with high confinement $H_{98y2} > 1.2$, $\beta_p \sim 2.5$ / $\beta_N \sim 2.0$, $f_{bs} \sim 50\%$ at high density $n_e/n_{GW} \sim 0.7$ and moderate $q_{95} \sim 6.7$ (shown in figure 6). By applying a mixture of 50% neon and 50% D_2 impurity seeding near the upper outer strike point, the peak heat flux is reduced by ~30% on the outer tungsten divertor plate in a high-β_p plasma with I_p = 400 kA, B_T = 2.4 T, and power injection of RF (~3.4 MW) and NBI (~5.4MW). During the impurity seeding feedback control phase, the total radiation power obtained

from bolometer diagnostics gradually reached the target radiation value of 0.9 MW and then kept in stationary state for a duration of > 2 s, longer than 5 current diffusion times, while the density was kept unchanged. Notably, the energy confinement quality was stably maintained at $H_{98y2} > 1.2$ during the radiation feedback control phase, showing good compatibility of core and edge conditions. All the profiles remained nearly the same. Both the ITB in electron temperature profile and edge pedestal structure were maintained during the feedback control phase. The demonstration of the compatible core and edge integration has provided confidence for future long-pulse operation at higher heating and current drive power in EAST.

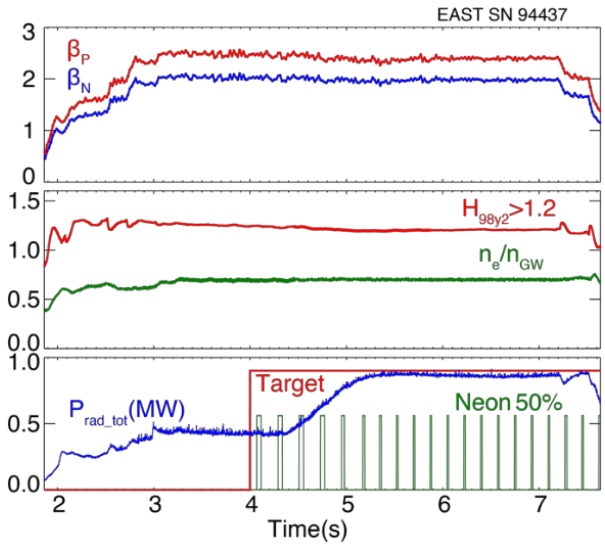

FIG. 6 Time histories of several parameters for high-β_p discharge with radiation feedback control in EAST. From top to bottom: poloidal beta, normalized beta, confinement enhancement factor H_{98y2}, the density normalized to Greenwald density n_e/n_{GW}, and plasma radiation feedback control using mixed impurity seeding (50% neon +50% D2).

3. ADVANCES IN ACTIVE CONTROLS OF DIVERTOR HEAT AND PARTICLE FLUXES IN SUPPORT OF STEADY-STATE OPERATION

3.1.Grassy-ELM regime with radiative divertor

A stationary high-confinement grassy ELM regime compatible with metal wall, low plasma rotation and feedback-controlled radiative divertor has been successfully achieved in EAST [16, 17], in which the conditions are generally projected for tokamak fusion reactors. Grassy ELMs with frequency f_{ELM} > 500 Hz have been accessed in a broad parameter space at relatively higher $q_{95} \sim 5.3$ and $\beta_p \sim 1.2$. Statistics analysis indicates that large and grassy ELMs could coexist in a critical region of $q_{95} \sim 5.3$-6.4, whilst for lower q_{95} of $q_{95} < 5.3$ large ELMs mainly occur [18]. The grassy ELM regime is characterized by a wide pedestal with a low-density gradient and a high-density ratio between the pedestal foot and top. Linear analysis indicates that the peeling-ballooning modes responsible for the burst of the grassy ELMs are not necessarily high-n modes or more localized than the type-I ELM

regime [19, 20, 21]. A nonlinear simulation with the BOUT++ code has revealed that the peeling boundary moves upward induced by a radially localized steepening of the pedestal pressure gradient after the initial pedestal crash. The working point falls into the stable region and the pedestal collapse stops [16]. This could be the underlying mechanism for the observed small ELM crash. In contrast, for large ELMs, the pedestal is much narrower and the pressure gradients are reduced immediately in the whole pedestal region after an initial pedestal crash. Then, the stabilizing effect by the pressure gradient is reduced. The peeling boundary shifts upward slightly, and the working point still remains in the unstable region. The pedestal collapse continues, finally leading to a large ELM. This understanding offers a new physics basis for mitigating ELMs in future steady-state fusion reactors.

In addition to natural grassy-ELM H-mode operation, the transition from mixed large and small ELMs to pure grassy ELMs has also been achieved with impurity seeding during the exploration of grassy ELM regime toward lower q_{95} in EAST [22]. As shown in figure 7, the discharge #80595 with q_{95} ~ 5.7 was operated at a lower and marginal q_{95} space where large and small ELMs can coexist. It is found that the ELMs become grassy with an increased frequency from f_{ELM} ~ 500 Hz to f_{ELM} ~ 1200 Hz after mixed impurity seeding with 20% neon and 80% deuterium. Moreover, the ELMs become even more grassy at a frequency of f_{ELM} ~ 1600 Hz after the second impurity seeding pulse. This provides a new method for the further exploration of grassy ELM regimes toward ITER-relevant low q_{95} in EAST. More importantly, the core plasma confinement maintains stably with β_p ~ 1.5, showing excellent core-edge integration with impurity seeding, similar to the results in high β_p scenario.

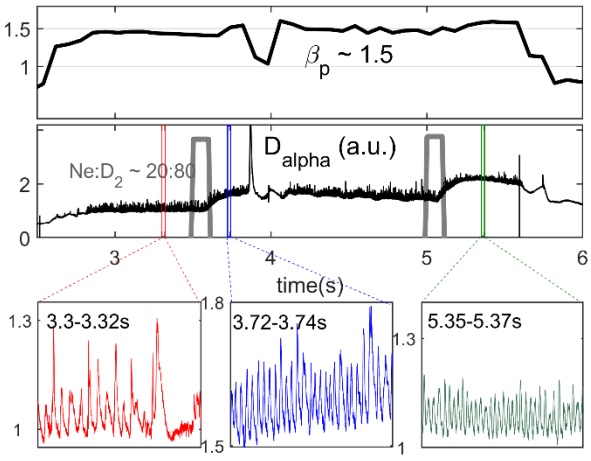

FIG. 7 Time histories of poloidal beta and D_α for grassy ELM discharge with mixed neon and deuterium seeding pulses labelled. Bottom panels from left to right are three time slices of D_α before and after impurity seeding to characterize the ELM frequency.

3.2. Active control of heat and particle exhaust

3.2.1. Divertor detachment feedback control

The divertor detachment is the most promising means for the active control of the steady-state heat flux and thus plasma-wall interactions (PWIs) at the target plates in future tokamak fusion devices such as ITER [23]. An excessively high heat flux can melt the divertor target plates, which induces material sputtering and erosion, posing a critical risk for the steady-state operation. A series of new detachment feedback control tools have been developed and successfully applied in EAST [24], in addition to the previous detachment control via divertor particle flux [25]. These methods can effectively reduce the heat load on the divertor target plates while still maintain good core confinement in H-mode plasmas simultaneously. EAST has achieved actively controlled detachment with $T_{e,div}$ = 5 eV and $H_{98y2} \geq 1.1$ in several H-mode scenarios, including normal ELMy H-mode, grassy ELMy H-mode and high β_p H-mode.

The electron temperature at divertor target (T_{et}) set at 5 eV, which is measured by the divertor Langmuir probes (Div-LPs), is used as an indicator for detachment. It is successfully demonstrated by this control scheme as illustrated in Fig. 8a for such a discharge in USN divertor configuration with favorable B_T (ion $\mathbf{B}\times\nabla\mathbf{B}$ drift towards the X-point, $\mathbf{B}\times\nabla\mathbf{B}\uparrow$) at B_T = 2.4 T, I_p = 400 kA. The line-averaged electron density is approximately 5.3×10^{19} m^{-3} and the total injected power (P_{inj}) is 2.5 MW. The monitored electron temperature comes from a Div-LP near the strike point on the upper outer divertor. The target T_{et} is pre-set to 5 eV (the red line in fig. 8(a1)). When T_{et} is > 5 eV, the neon impurity is seeded in the form of pulses at the upper outer divertor until it reaches the target value. The seeding rate is regulated by pulse frequency with a fixed valve open time. A mixture gas containing 50% neon and 50% deuterium is applied in this experiment. The radiated power (P_{rad}) in the total bulk plasma is measured using an the absolute extreme ultraviolet (AXUV) photodiode array. Increase of the radiated power is accompanied with decrease of the electron temperature at the divertor target, indicating the reduction in the energy reaching the divertor target. The electron temperature at the divertor target is stably controlled in a stationary status for several seconds, when the radiative power remains also almost stationary. Note that the seeding impurity does not reduce the plasma stored energy and the core confinement. For shot#85293 by neon seeding, the plasma stored energy (W_{MHD}) and H_{98y2} increased slightly, providing good core-divertor compatibility. As a comparison, Argon is used instead of Neon and shows more efficient for achieving divertor detachment, but with a slight loss of confinement. A detailed discussion has been reported in ref. [26].

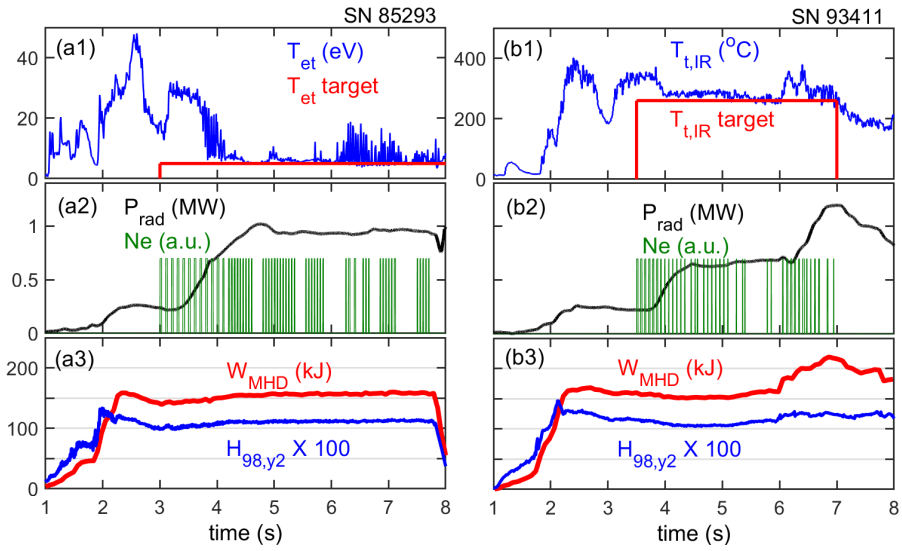

FIG. 8 Detachment feedback control utilizing divertor electron temperature (a) and surface temperature of the target plate (b), respectively. From top to bottom, $T_{et}/T_{t,IR}$ near the outer strike point of the upper divertor, the red line indicates the target for the controller; the radiation power and the voltage signal of the piezo valve for neon seeding; The plasma stored energy and the confinement improvement factor H_{98y2}.

The divertor surface temperature feedback has also been successfully demonstrated in EAST [27], as shown in Fig. 8 (b). The peak surface temperature of the divertor target plate ($T_{t,IR}$) is measured by an infrared (IR) thermography and inputted to the plasma control system in real time, in which the time resolution of $T_{t,IR}$ is 100 Hz. Note that the temperature measured by IR camera, $T_{t,IR}$, is the surface temperature of the divertor plate, different to the electron temperature of the plasma (T_{et}, measured by Langmuir probes) on the divertor target plate. Similar to the control method mentioned above, the neon is seeded when the peak surface temperature is higher than the set target value. The basic plasma parameters are as follows: $n_e \sim 4.8\times10^{19}m^{-3}$, P_{inj} = 3.0 MW, I_p = 400 kA, and B_T = 2.4 T. The surface temperature is significantly reduced at 3.9 s because of the neon seeding. At 6.0 s, the surface temperature of the target plate and radiated power suddenly increase because of the input power of NBI. In addition, the plasma-stored energy and the confinement improvement factor indicates that the radiative divertor does not degrade the core confinement significantly. Note that in Fig 8 (b2), the drop of $T_{t,IR}$ after 7s is due to the movement of strike point, detailed in Ref. [27].

In addition, a synergistic control of the X-point radiation and electron temperature on the divertor target has been developed in grassy-ELM H mode in EAST to improve reliability and stability of detachment control needed for long pulse operation under different regimes. Here, the radiation value is from one AXUV channel with the viewing line across the X-point rather than the total radiation power. It has been experimentally found that the AXUV channel near the X-point, where a steep gradient in the radiation profile is present, is sensitive to both the pedestal performance and T_{et} around upper outer strike point. In the feedback control scheme, T_{et} around upper outer strike point is used to

judge the onset of the detachment. Once T_{et} reaches the set value, the feedback scheme switches to the control of one channel of AXUV radiation near the X point. Fig. 9 shows a typical synergistic control discharge and the key plasma parameters are $n_e \sim 4.6\times10^{19}$ m^{-3}, P_{inj} = 3.0 MW, I_p = 400 kA, B_T = 2.4 T. In the USN discharge (shot 87887), the target of T_{et} is set to 8 eV. With mixed gas (50% Ne and 50% D_2) seeding from the upper outer divertor target, the target value was achieved in about 4.5 s. At this moment, the AXUV channel 59 is switched as the control parameter. Once the AXUV value is lower than the AXUV target, the neon impurity is seeded to maintain stable detachment. There is no drop in plasma stored energy and the confinement improvement factor H_{98y2} is always >1. Grass-ELM regime is characterized by good core confinement and small transient heat flux on the divertor target, only ~ 1/20 of the large type-I ELMs. The newly developed detachment feedback control scheme thus offers a promising operation mode for the control of both ELM-induced transient and steady-state divertor heat flux with good core performance. In the future, active detachment feedback control compatible with core confinement in long-pulse plasmas with a high-power input is planned to be demonstrated in EAST, along with extending the joint DIII-D/EAST detachment experiments [28] to more reactor-relevant conditions.

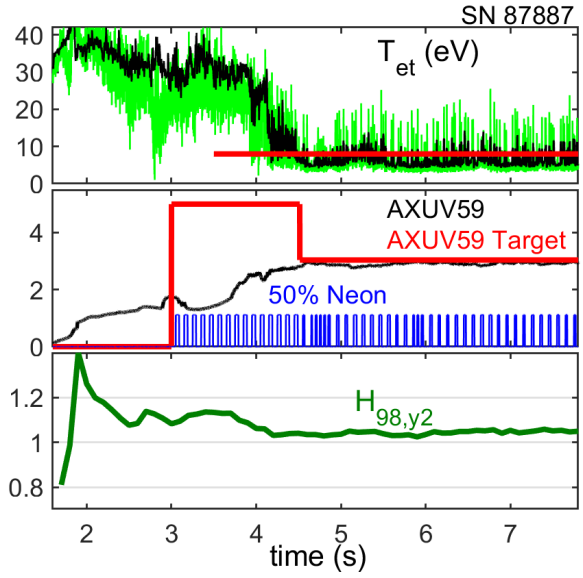

FIG. 9 Feedback control of divertor neon seeding in a grassy-ELM discharge in EAST, shot #87887. From top to bottom, electron temperature (T_{et}) near the outer strike point of the upper divertor, the red line indicates the T_{et} target for the controller; AXUV channel59 (black) measuring radiation mainly near the upper X point, the AXUV59 target (red) for the controller, the voltage signal of piezo valve for neon seeding (blue); the confinement improvement factor H_{98y2}.

3.2.2. Development of flowing liquid Li limiters

Lithium, which serves as plasma facing material in fusion devices, can solve several key issues including particle recycling and impurity control, which is gaining increasing attention [29]. Four generations of flowing liquid Li limiters (FLiLi) have been developed in EAST [30, 31]. The first

liquid Li limiter, using stainless steel (SS) layer as substrate in a thickness of 0.1 brazed on copper heat sink and one EM pump for Li driving, was tested in EAST in 2014. The second generation, in which a 0.5mm SS substrate on copper heat sink and two EM pumps are used for improvement of liquid Li fractional surface area coverage of the limiter plate, the elimination of surface erosion, was tested in EAST in 2016 [32]. The third generation, using a molybdenum substrate for improvement of Li wetting and erosion resistant, was tested in 2018 [33]. The fourth generation, based on the concept of liquid metal infused trenches (LiMIT), i.e., using a thermoelectric MHD force to drive liquid Li flow along the surface trenches with ~2 mm × 1 mm（length × depth）to enhance heat removal capacity of liquid Li, was successfully applied in EAST in 2020. The FLiLi is designed for a flow rate of 2 cm^3/s, which pumps ~10^{22} D/s during discharges. The limiter is composed of a distributor, a guide plate, a collector and an EM pump. Liquid Li is driven using an in-vessel direct current electromagnetic pump from the collector to the distributor. Subsequently, it flows from the holes of the distributor and across the plate. Finally, it is collected by the collector, forming a closed recirculation loop. FLiLi could be smoothly moved from outside of EAST to the vacuum vessel (low field side (LFS)) with a mechanical drive assembly employed in the Li and plasma evaluation system (LiPES) platform. The distance between substrate plate and the separatrix is approximately in the range of 0-5 cm. The limiter temperature was operated in the range 330-380□ over an auxiliary heating power range of 2-8.3 MW with LHW, ECH, and NBI.

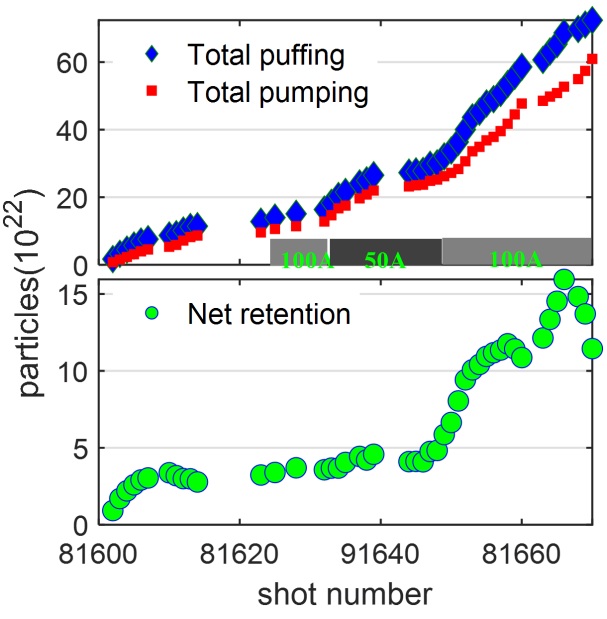

FIG. 10 Retained D particles during FLiLi limiter plasma discharges in EAST.

In EAST, Li coating was used as a routine wall conditioning method. However, the absorption of the fuel particles by Li coatings decreases gradually, and recycling gradually increases over series of discharges [34]. The maximum net amount of deuterium retained reached ~0.8 g, corresponding to

12% deuterium in the Li. During FLiLi operation, the D_α emission normalized by the density and/or neutral pressure from upper and low divertors gradually decreased with increasing Li emission from FLiLi. Gas balance analysis confirmed a progressive increase in the fuel retention: the retention ratio, defined as the fraction of the fuel retained on the walls divided by the total injected fuel, increased from -0.8 to 0.55 with repeated FLiLi insertion. As shown in Fig. 10, a gradual increase of D retention was observed during FLiLi operation. Compared with daily pre-run evaporative Li coatings, the divertor D_α emission was ~3 times lower. This observation qualitatively confirms that the FLiLi provided fresh, unreacted Li during the discharge for continuous particle control, thus avoiding the normal wall saturation that occurs in long-pulse operations. Because of the reduced recycling, the pressure profiles gradually moved inward to reduce the pedestal pressure and gradually mitigate ELMs [35]. ELMs were largely eliminated during Li burst in the H-mode plasmas with pure RF heating. The duration of the ELM mitigation phase was extended in recent FLiLi experiments, which may be beneficial for controlling the ELM heat flux in future fusion reactors.

3.3.ELM control

3.3.1. ELM suppression with divertor impurity seeding

A simultaneous control of transient large ELMs and stationery divertor heat load in a metal wall environment is crucial for steady-state operation of a tokamak fusion reactor. A new scenario for ELM suppression compatible with radiative divertor has been demonstrated in EAST (shown in figure 11) [36]. An n = 1 mode along with its harmonics, initiating from the oscillation of a radiation belt on the high-field side SOL near the X point, is excited during CD_4 seeding from the upper divertor near the outer strike point in the H-mode plasmas at a sufficiently high impurity concentration. As shown in figure 11, CD_4 seeding is set to be constant and the mode appears after a short time interval. Robust ELM suppression has been achieved in the presence of this mode over a wide q_{95} range of 4.5-6.5 (I_p = 400-600 kA and B_T = 2.25-2.47 T) and a wide heating power range with source power ranging from 3 MW to 9 MW. Along with ELM suppression, a complete detachment at the inner target and a partial detachment at the outer target with target electron temperature T_{et} < 10 eV has been achieved without degrading the global energy confinement. The plasma stored energy is maintained nearly constant. The dominant pedestal fluctuations, edge coherent mode (ECM), in the ELMy phase are significantly reduced during CD_4 seeding, as shown by the polarimeter-interferometer measurements. Furthermore, the active feedback control of either T_{et} or divertor radiation with impurity seeding has been developed and successfully demonstrated in this regime, detailed in ref. [37].

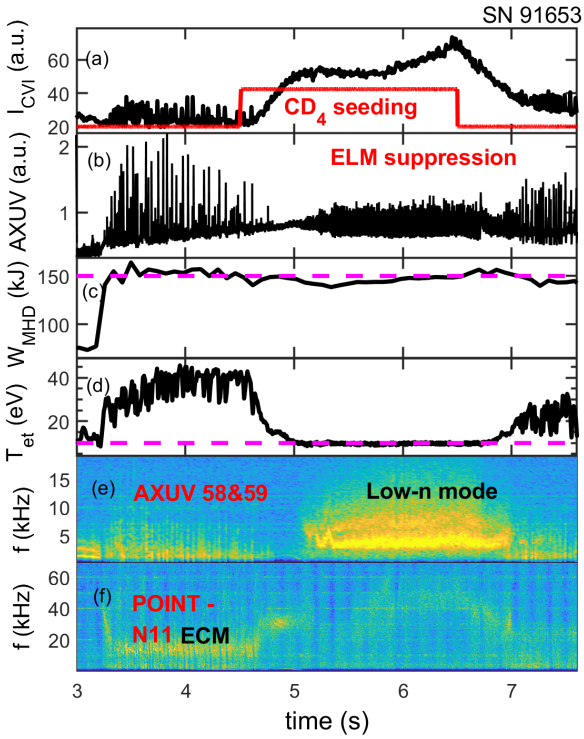

FIG. 11 ELM suppression and divertor detachment induced by CD_4 seeding. From top to bottom, Carbon radiation signal (black) and CD_4 seeding (red); AXUV signal across the X point, stored energy; T_{et} near the outer strike point; cross-correlation frequency spectrum of AXUV; density fluctuations from the POINT system.

Robust ELM suppression was observed when boron powder was injected above the upper X-point in the upper-single null discharges. The solid boron powder (averaged diameter ~70 μm) was injected using a new generation impurity powder dropper, which was developed by PPPL [38]. Figure 12 shows a direct comparison of the two dedicated discharges with the same plasma setup, except for the one with B powder injection and ELMs suppressed, while the other one without the B powder injection and ordinary type-I ELMs. B injection was initiated at approximately 1.7 s, leading to BV emission from the plasma (Panel (a), orange curve). The ELMs, visible as spikes in the upper divertor D_α emission in the reference discharge, were eliminated with B injection (Panel (b)). The line-average density was matched (Panel (c)) by moderately reducing the feed-forward gas puffing to counteract the electron fueling from B powder injection. The plasma stored energy was modestly higher in the discharge without ELMs (Panel (d)). Along with the ELM elimination came destabilization of the edge-localized oscillation with several harmonics, which was confirmed to provide a continuous particle exhaust to maintain constant density and avoid impurity accumulation [39, 40].

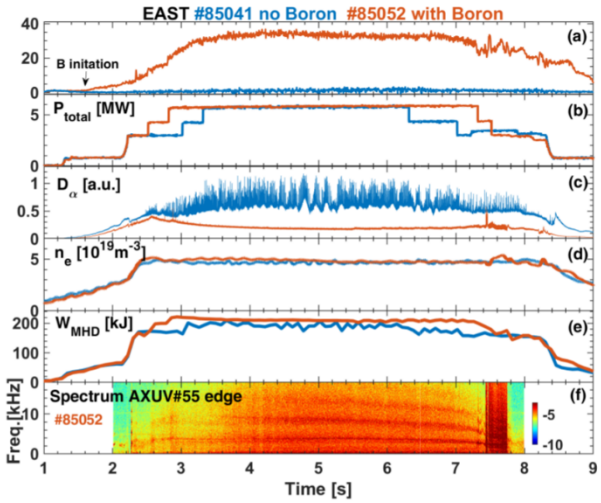

FIG. 12 Comparison of reference ELMy discharge without B powder injection (blue) and ELM suppression discharge with B powder injection (orange): (a) intensity of BV emission measured by extreme ultraviolet spectroscopy, (b) total heating power, maximum heating power ~6MW, mixed with NBI and RF heating (c) D_α emission from the upper outer divertor, (d) central line-averaged density, (e) stored energy from equilibrium reconstructions W_{MHD}, (f) auto power spectrum of an AXUV viewing the edge plasma

The boron-induced ELM suppression was demonstrated over a wide range of engineering and plasma parameters: with both favorable and unfavorable ion $\nabla\mathbf{B}$ drift directions, a q_{95} range of 4.4–7.2, a n_e/n_{GW} range of 0.24–0.87, an H_{98y2} factor range of 0.7–1.3, a plasma-stored energy range of 115–254 kJ, with pure radio frequency heating up to 5.8 MW, and with combined RF+NBI up to 7.5 MW [41]. In addition to the use of boron, similar results have been observed in EAST when using neon, argon, helium, and lithium seeding [42] when the impurity concentration exceeds a certain threshold. Similar observations on ELM suppression by impurity injection using neon, Li and Boron powder have been also reported in ASDEX-Upgrade, DIII-D and KSTAR [43, 44, 45]. The new ELM control approach appears to be insensitive to impurity species, q_{95}, heating power, and plasma toroidal rotation. It shows good compatibility with the stationary divertor heat load control, which thus offers a highly promising plasma operational regime suitable to achieve long-pulse high-performance H-mode operation in EAST. It may be potentially applicable to future tokamak fusion reactors, as a solution to control ELM-induced transient divertor heat loads.

3.3.2. Simulation on the control of ELM and edge turbulence by RF waves

In EAST experiments, various methods have been actively used to control ELMs effectively. During those ELM control phenomena, the appearance of the coherent modes in the pedestal region is found to be accompanied with the mitigation and suppression of ELMs. For example, the ECMs are commonly found during the small/no ELM H-mode regime on EAST for the relatively higher pedestal collisionality [46, 47]. For the lower collisionality cases, the magnetic coherent modes (MCMs) are reported in reference [48]. Therefore, understanding the interactions between those coherent modes and ELMs becomes important for the ELM control in the long pulse operations. For

simplicity, the pedestal coherent modes (PCMs) are used to represent the coherent modes in the pedestal region mentioned above in the following section. We extend the capabilities of the BOUT++ code in order to simulate the interactions between PCM and ELMs. Notably, the drift effects, such as **E×B** and diamagnetic drifts, are included in the BOUT++ simulations [49]. The EAST ELMy H-mode discharge #77741 at 3.5s is used as the simulation equilibrium. The EAST ELMy H-mode discharge #77741 at 3.5s is used as the simulation equilibrium. The ELM frequency is around 20-30Hz, and the energy loss $\Delta W_{dia}/W_{dia}$ by the ELM burst from the diamagnetic diagnostic is ~ 3.9%. The stability analysis shows that the equilibrium is outside the ideal peeling-ballooning stable boundary, indicating that the ELM size belongs to the large ELM range. After the ELM crashes, the coherent mode can be obtained during the nonlinear saturation phase. The contributions from the electromagnetic and electrostatic coherent modes are separately analysed. If only the magnetic component of the PCM is considered, which is set as the additional background magnetic flutter, the mechanism is similar to the topology change effects, and the amplitude of the ELM fluctuation can be decreased by up to 28% [50]. The higher amplitude of the background flutter leads to the smaller ELM size. To consider the electrostatic effects on ELMs, the PCM is added to the model as the background pressure perturbation. The simulation results show that the ELM size is effectively mitigated by approximately 45%.

Figure 13 shows the comparisons between the cases with and without the PCM. The profiles at the outer midplane at the initial time, 1000 Alfvén time, and 1800 Alfvén time are plotted in Panels (a) and (c). Compared with the w/o PCM case in Panel (a), the pressure profile in the PCM case is crashed less and later, and the crash region is largely constrained outside ψ_N = 0.86. The time evolutions of the dominant mode spectrum are shown in Panels (b) and (d). The mode spectrum with PCM in Panel (d) is wider than the w/o PCM case. This indicates there are more mode couplings for the case with PCM. The mechanism of the ELM mitigation by PCM is related to the three-wave nonlinear interactions. The existence of the background PCM helps enhance the three-wave couplings and effectively reduce the phase coherence time (PCT) between the pressure and potential [51]. The linear growth time is limited by the shortened PCT; therefore, the amplitude of the fluctuations cannot increase to the original level, which leads to the smaller amplitude of the ELM energy loss. For a detailed understanding of the effects on ELM, the phase angle, amplitude, and dominant toroidal mode number are scanned. The results show that these parameters are insensitive to the effects of ELM mitigation. The phase angle can affect the ELM energy loss after the crash, but in the saturation phase, the ELM size still becomes the same. When the amplitude of the PCM is higher than the initial perturbation of the ELM, the ELM will be mitigated to a similar value, since the mode coupling leads to a similar amplitude of the fluctuation. If the dominant toroidal mode number of the PCM is different from the intrinsic dominant mode of the ELM, the modes are coupled from the linear

growing phase, and a similar amplitude will be obtained in the saturation phase. These results show that the ELM can be easily mitigated by the coherent modes in the pedestal region [52].

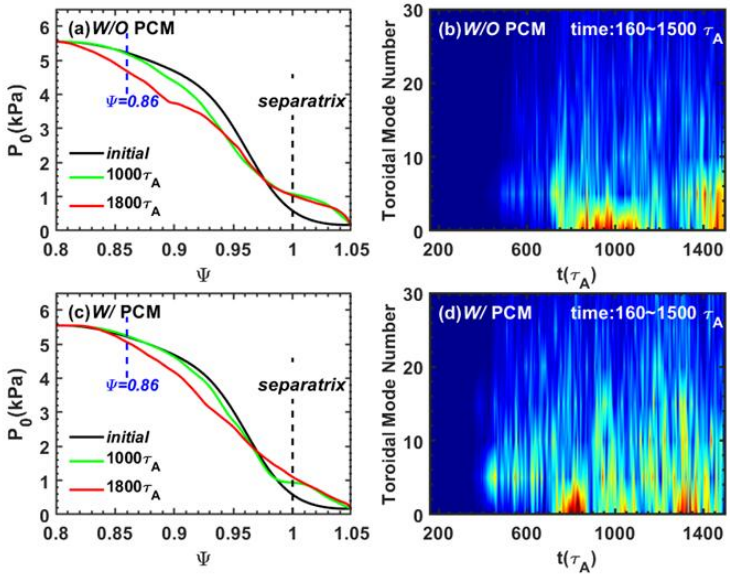

Fig. 13 (a) Pressure profiles at outer midplane w/o PCM case. The black curve indicates the initial profile; the green is at 1000 Alfvén time, and the red is at 1800 Alfvén time. (b) Time evolution of the dominant mode for the w/o PCM case. (c) Pressure profiles at the outer midplane in the PCM case. (d) Time evolution of the dominant mode in the PCM case.

4. PROGRESS IN PHYSICS-RELATED STUDIES FOR ITER

4.1.ELM control by RMPs

A full suppression of ELMs using n=4 resonant magnetic perturbations (RMPs) has been demonstrated under ITER relevant condition on EAST for the first time (n is the toroidal mode number of the applied RMPs) [53]. This is achieved in plasmas with a low input torque and the use of the tungsten divertor, thus also addressing significant scenario issues for ITER. The normalized parameters of the target plasma for these experiments in EAST are specifically chosen to be relevant to the ITER type-I ELMy H-mode (Q = 10) scenario [54]. In these experiments the NBI torque is approximately $T_{NBI} \sim 0.44$ N·m, which extrapolates to 14 N·m in ITER (compared with a total torque input of 35 N·m when an NBI of 33 MW is used for heating). ELMs are completely suppressed using n = 4 RMPs with odd parity (opposite phases in the upper and lower rows of coils current) in EAST but not when even parity is applied to a type I ELMy H-mode plasma with $q_{95} \approx 3.65$ and $\beta_N \sim 1.5$-1.8, similar to that in the ITER Q = 10 scenario. The electron and ion temperature are very similar with $T_{i0} \approx T_{e0} \approx 2$ keV. Under these conditions, energy confinement does not drop significantly (<10%) when ELM suppression is achieved compared with the ELMy H-mode conditions, while the core plasma tungsten concentration is clearly reduced as shown in Figure 14. This is very different from previous

observations using low n (n=1 and 2) RMPs in EAST with high q_{95} ($\geq$ 5), in which the plasma stored energy was significantly reduced (>20%) [55, 56].

The threshold n=4 RMP current for full ELM suppression is approximately 2 kA (four turns). Suppression windows in both q_{95} and plasma density are observed; in addition, lower plasma rotation favours access to ELM suppression. Outside the q_{95} and density window only ELM mitigation, not suppression, is observed. ELM suppression is achieved in a narrow q_{95} window in [3.6, 3.75] with odd n=4 RMP configuration with a continuous q_{95} decrease (Ip ramp-up). ELM suppression is maintained up to 60% of n_{GW} by feedforward gas fuelling after suppression. Interestingly, there is not only an upper density but also a lower density threshold for ELM suppression of 40% n_{GW}. The observed ELM suppression window is consistent with the peak in the modelled edge stochasticity using the MARS-F code [57]. These results expand physical understanding and demonstrate the potential effectiveness of RMPs for reliably controlling ELMs in future ITER Q=10 plasma scenarios.

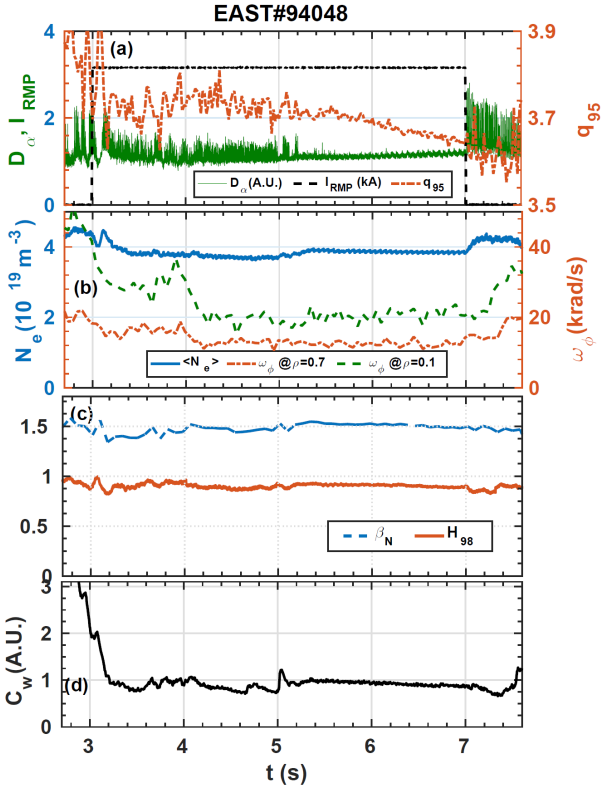

FIG. 14 *Full suppression of ELM by odd n=4 RMP in EAST discharge 94048. From top to bottom, (a) D_α emission (green line), RMP coil current (black dashed line) and q95 (orange dashed-dotted line), (b) line average electron density (blue line) and toroidal plasma rotation at ρ=0.1 (green dashed line) and ρ=0.7 (orange dashed dotted line) respectively, (c) H_{98y2} (solid orange line) and normalized beta (blue dashed line), and (d) core tungsten concentration.*

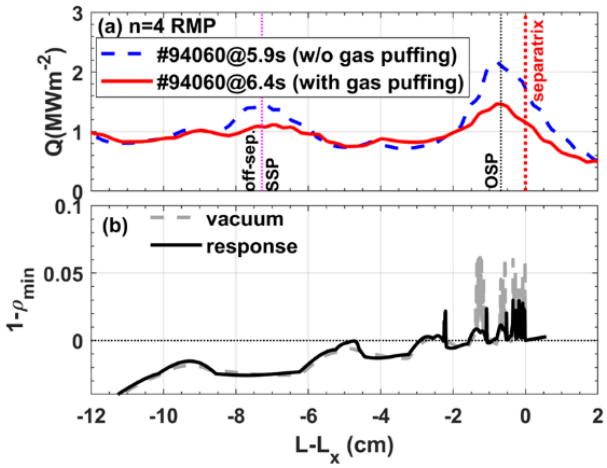

FIG. 15 (a) *Comparison of heat flux profiles without (the blue dashed line) and with (the red solid line) gas puffing during n = 4 RMP ELM suppression. (b) The modelled divertor field line penetration depth at the corresponding toroidal angle by TOP2D in vacuum approximation (the grey dashed line) and that taking into account the plasma responses calculated by MARS-F (the black solid line).*

Experiments have also been carried out in EAST to study ITER relevant scenario integration issues of the ELM control in H-mode plasmas by the application of RMPs, which have a large impact on the execution of the ITER research plan [58]. These include the impact of ELM mitigation and suppression on particle and energy confinement and its dependence of the toroidal spectrum of RMP, compatibility with low input torque operation, pellet fuelling and control of the divertor power fluxes by gas fuelling and impurity seeding. Accessing to high recycling and radiative divertor conditions while maintaining ELM suppression has been demonstrated in EAST and this is effective in reducing power fluxes to the divertor strike points in near-separatrix lobes as shown in figure 15 [58, 59]. The reduction of power fluxes in off-separatrix lobes is effective in the n=4 RMP application case in which the magnetic topology modelling with plasma responses reveals a shallow penetration into the plasma region of field lines connected to these lobes modelled by the TOP2D code [60, 61]. These results in EAST support the use of high n 3-D fields for ELM control in the low-torque ITER baseline scenario. It will help strengthen the physical basis for achieving high Q integrated operation scenario in ITER. While impurity seeding is effective to both ELM mitigation/suppression and divertor heat flux distribution, whether there is a synergistic effect of RMPs and impurity seeding for the ELM mitigation and suppression will be an open research topic important for ITER baseline operation.

4.2.Helium plasmas

The helium plasmas have been demonstrated for the first time in EAST under the condition of pure RF heating and ITER-like tungsten divertor, which advances the physical understanding in support of the ITER non-nuclear operational phase. Pure helium was used to build up target plasma, while D2 gas puffing was used to control the helium concentration during the experiments. The helium (C_{He}) concentration in the plasma is confirmed to play a critical role in H-mode operation, as a higher

concentration increases the H-mode threshold power and deteriorates the energy confinement in the H mode [62]. At lower C_{He} (C_{He} < 70%), EAST achieved a stationary type-I ELMy H mode over 80 times of the energy confinement time with the energy confinement slightly above H_{98y2} scaling (H_{98y2} ~ 1.1) using pure RF power.

4.2.1. Helium plasma H-mode operation

The first H-mode in helium plasma was accessed by optimizing the plasma shape to improve LHW coupling [63]. The results show that a higher possibility of stationary type-I ELMy H-mode comes with lower C_{He} and edge safety factor q_{95}. Figure 16 shows an example of the high-performance H-mode discharge (I_p ~ 0.5 MA, B_T = 2.4 T, q_{95} ~ 5.5) with characteristic of type-I ELM behavior (f_{ELM} ~ 10–30 Hz) from 3.5 s to 8.0 s. The plasma configuration is a USN with the strike points located on the vertical targets of the tungsten divertor. With increasing C_{He} under identical experimental conditions, the ELM behavior evolves into higher frequency ~400 Hz or is even absent. Experiments on the high-energy confinement operation have shown that the global energy confinement time in He is approximately 30% lower than in D, similar to AUG results [64]. For both the ion species, the energy confinement time steadily increases with the central line-averaged density in the range of 2–5×10^{19} m^{-3}. Under a fixed plasma condition (I_p = 0.5 MA, B_T = 2.4 T, n_e = 4.3×10^{19} m^{-3}, and P_{inj} = 4 MW), C_{He} lowered by active D gas puffing gradually improves the H-mode performance [63].

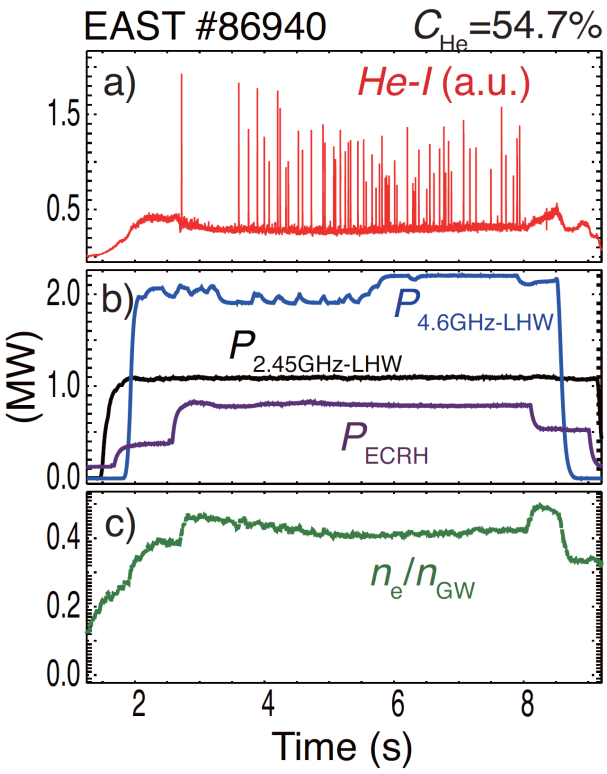

FIG. 16 *Time traces of plasma parameters of type-I ELMy H-mode discharge. From top to bottom: He-I line emission count, the injected power of LHW and ECRH, and the density normalized to Greenwald density n_e/n_{GW}.*

One of the essential tasks in ITER He operational phase is to test the ELM control techniques, such as the resonant magnetic perturbation (RMP) technique. In EAST, successful ELM suppression by n = 1 RMP in He plasma with pure RF-heating power of 4.3 MW and q_{95} of 5.8 was first demonstrated. A strong density pump-out effect was observed during the ELM suppression period, while the reduction in the plasma store energy is approximately 8% lower than the D discharges. By ramping up the RMP current, the threshold current of n = 1 RMP required to suppress ELMs was found to be only 1 kA. Moreover, there was no clear n = 1 RMP spectra dependence. ELM suppression could be achieved at a similar threshold current with diverse RMP spectra.

ELM suppression was also achieved by boron powder injection technique in He plasma with pure RF heating [63]. Boron powder was injected at the upper X-point using a new-generation impurity powder dropper [39]. During the ELM suppression phase with boron injection, the plasma-stored energy and electron density were largely the same as before, and the energy confinement did not deteriorate. No impurity accumulation was found either, indicating little impact on the core plasma performance. In addition, the injection of boron powder above the minimum for ELM suppression coincides with the occurrence of an edge harmonic oscillation phenomenon, which was observed by various diagnostics.

4.2.2. Plasma-wall interactions during helium plasma operation

As EAST has been assembled with an ITER-like tungsten mono-block divertor, plasma–wall interaction studies can provide good references for the ITER He operational phase. Divertor detachment in He-D mixed plasma, with CHe ranged from 40% to 80%, has been achieved using density ramps for the first time [65]. The divertor detachment is similar to that in D operations in that the inner target detaches first with the rollover of the particle flux and the reduction in the electron temperature in the $\mathbf{B}\times\nabla\mathbf{B}$ drift direction towards the X-point. Furthermore, new results have shown that the detachment begins at a higher upstream density than in previous equivalent deuterium plasmas at the same power to the scrape-off layer. The experimental result shows that the density of the detachment onset increases with the heating power, as shown in figure 17. Low levels of neon impurity seeding can help achieve divertor detachment at a lower density. An active feedback control of the radiation power by Ne seeding can help approach divertor detachment without deteriorating the core plasma performance [66]. Tungsten erosion in He discharges has also been studied using a multichannel spectroscopy system applied to observe the 400.9 nm WI emission intensity in the upper outer divertor region [67]. The tungsten erosion rate in He plasmas is much higher than that in D plasmas. The inter-ELM W erosion rate in He is more than 3 times that in D under similar divertor conditions because of the higher W sputtering yield of He ions. The intra-ELM W sputtering source for type-I ELMs in He plasma increases nearly linearly with the ELM frequency, similar to the D campaign results from DIII-D [68] and JET [69].

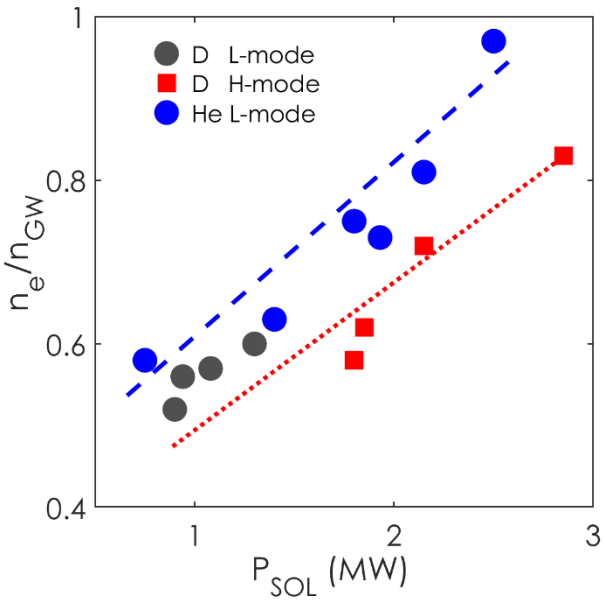

FIG. 17 The ratio of divertor detachment threshold density to Greenwald density as a function of power to the scrape-off layer PSOL for He (blue) and D (red) discharges.

Sample exposures have been successfully carried out with He plasma using the outboard midplane manipulator MAPES to study material migration processes. A proxy tile for the first wall panels in ITER with two different material coatings, namely carbon and aluminum, on different sides of the plasma wetted area, has been exposed in the L-mode He plasma, thus avoiding the effects of chemical erosion. No net material deposition in the shadowed regions was found, similar to previous experiments [70]. A known quantity of $^{13}CD_4$ was injected and traced using graphite samples in both the He and D plasmas to study material migration in the main chamber wall and the effect of chemical erosion on C redeposited layers. A redeposited layer was formed close to the injection point after the exposure, and the direction of the material migration was dominated by the **E**×**B** drift. A post-mortem nuclear reaction analysis showed an unexpected result in that the ^{13}C deposition fraction in D was approximately 50% higher than that in He, indicating a higher physical sputtering rate by He than the chemical erosion rate by D [71].

5. SUMMARY AND FUTURE PLANS

Significant progress has been made in the development and understanding of the relevant physics with respect to the long-pulse steady-state operation in EAST since the last IAEA FEC in 2018. A long-pulse steady-state H-mode of 60 s with small ELMs and a good confinement performance (H_{98y2} ~ 1.3) was demonstrated through an integrated operation. The long-pulse discharge reaches a wall thermal and particle balance through an ITER-like tungsten divertor. Active control of divertor radiation has been successfully integrated into the high beta H-mode plasma scenario without a degradation of the plasma confinement ($H_{98y2} > 1.2$) at high density ($n_e/n_{GW} \sim 0.7$) and moderate edge safety factor ($q_{95} \sim 6.7$). The peak heat flux on the tungsten divertor was reduced by ~30% with active

impurity seeding of a mixture of 50% neon and 50% deuterium. The grassy-ELM regime has been extended to the normalized parameter space designed for the CFETR 1GW fusion power operation scenario. This regime exhibits good compatibility with high f_{bs} and fully non-inductive operation.

Several feedback control schemes have been developed to achieve sustained detachment with good core confinement. This includes control of total radiation power, target electron temperature, and particle flux measured by divertor Langmuir probes or a combination of the control of target electron temperature and AXUV radiation near the X point. A flowing liquid lithium (FLiLi) limiter plate has been successfully assembled and tested. Robust ELM suppression by Boron powder injection and CD_4 fuelling without confinement degradation or even with confinement improvement has been achieved in a wide parameter range. In addition, simulation results from BOUT++ confirm that ELM can be mitigated by the coherent modes in the pedestal region. Full suppression of ELMs by using n = 4 RMPs has been demonstrated for ITER for the first time in low input torque plasmas. For the first time, EAST has been operated with helium to support the ITER needs. Divertor detachment is more difficult to achieve in He than in D. The inter-ELM W erosion rate in He is about 3 times that in D with similar divertor conditions, while the intra-ELM W sputtering source shows a strong positive correlation with the ELM frequency.

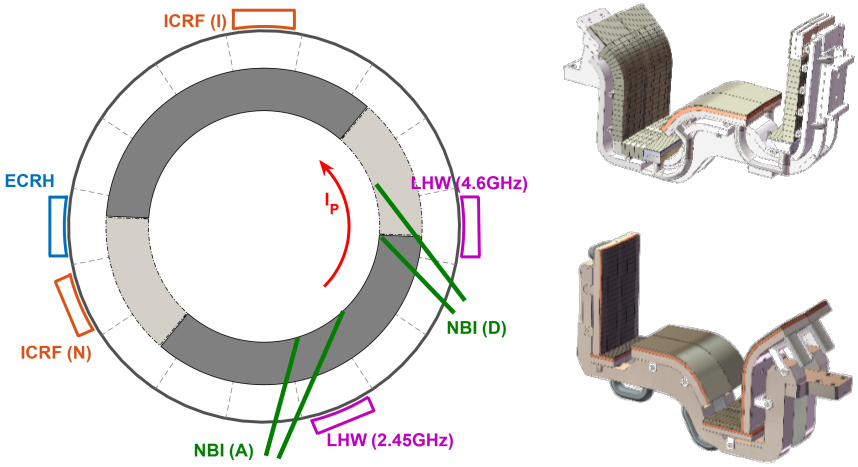

FIG. 18 Top view with toroidal locations of heating/CD systems in EAST (left); a divertor module with a monoblock structure (top); and a divertor module with a flat-type structure (bottom).

More heating and current powers and flexible power mix are required to achieve a very long-pulse, higher β_P and β_N plasma operation at ITER and CFETR relevant q_{95}. A further extension of the ECH system with an additional gyrotron is installed and will give more power for heating, current drive and profile control. Two 1MW new dual-frequency (140/105GHz) gyrotrons will be available in 2022, which allow extension of plasma operation regimes toward low q_{95} and high β_N at lower toroidal field. The existing full active multijunction (FAM) launcher will be replaced by a passive active multijunction (PAM) with active cooling for the 2.45 GHz LHCD system. With this new launcher, the

density for optimum coupling will be as low as 3×10^{16} m^{-3}, which lies below the cut-off value. Previous ICRF in port B has been moved to port N to minimize the magnetic connected area of antenna with the launcher of 4.6 GHz LHW system. A new two-strap ICRF antenna with lower k|| spectrum is just installed on port N to improve power coupling at lower plasma density. Moreover, the previous counter-current NBI system has been changed in the co-current direction for more efficient heating and current drive with eliminating a large fraction of the fast-ion losses.

Until April 2021, the EAST lower divertor has completed the upgrade from graphite divertor to tungsten divertor. The lower divertor has totally 48 modules, of which three-quarters use the ITER-like mono-block structure as the target plate, and the other quarter use the flat-type structure [72] as the target plate as comparison of different technologies, shown in figure 18. The installation accuracy of all divertor modules reaches ±0.5mm, and all target plates have large chamfers to avoid leading-edge. After upgrading, the steady-state heat exhausting capacity of the lower divertor is increased from 2 $MW\cdot m^{-2}$ to 10 $MW\cdot m^{-2}$, which provides support in future long-pulse high power exhausting experiments with ~10 MW power injection for >100s on EAST.

ACKNOWLEDGMENTS

This work was supported by the National Key R&D Program of China under Grant Nos. 2017YFE0301100, 2017YFE0301300, 2017YFE0301205, and 2018YFE0303104; the National Magnetic Confinement Fusion Energy R&D Program under Grant Nos. 2019YFE03030000, 2019YFE03040000, 2019YFE03070000, 2019YFE03010002, and 2019YFE03020004; and the National Key Research and Development Program of China under Grant No. 2017YFA0402500.

Appendix

The EAST Team

Yuntao Song[1], Baonian Wan[1], Jiangang Li[1], Yuanxi Wan[1], Xinchao Wu[1], Fukun Liu[1], Junling Chen[1], Jiansheng Hu[1], Guosheng Xu[1], Kun Lu[1], Xiaodong Zhang[1], Peng Fu[1], Houyang Guo[1,15], Yunfeng Liang[1,32], Xianzhu Gong[1], Bingjia Xiao[1], Yu Wu[1], Xiang Gao[1], Damao Yao[1], Nong Xiang[1], Liqun Hu[1], Jiafang Shan[1], Yanping Zhao[1], Guangnan Luo[1], Chundong Hu[1], Jiefeng Wu[1], Biao Shen[1], Zhenshan Ji[1], Ge Gao[1], Yiyun Huang[1], Liuwei, Xu[1], Qiyong Zhang[1], Ming Zhuang[1], Junyu Zhao[1], Bin Cao[1], Lei Cao[1], Jiafeng Chang[1], Kaiyun Chen[1], Ran Chen[1], Yebin Chen[1], Anyi Cheng[1], Yong Cheng[1], Yu Dai[1], Wei Deng[1], Xu Deng[1], Bojiang Ding[1], Fang Ding[1], Rui Ding[1], Siye Ding[1], Shijun Du[1], Yanmin Duan[1], Jianqiang Feng[1], Kaifu Gan[1], Daming Gao[1], Qingsheng Gao[1], Wei Gao[1], Yongqi Gu[1], Yong Guo[1], Xiaofeng Han[1], Ailan Hu[1], Chang Hu[1], Guanghai Hu[1], Huaichuan Hu[1], Liangbin Hu[1], Qingsheng Hu[1], Yanlan Hu[1], Zhenhua Hu[1], Juan Huang[1], Liansheng Huang[1], Ming Huang[1], Ronglin Huang[1], Xiang Ji[1], Hua Jia[1], Caichao Jiang[1], Yinxian Jie[1], Songqing Ju[1], Defeng Kong[1], Changzheng Li[1], Erzhong Li[1], Guoqiang Li[1], Jiahong Li[1], Jun Li[1], Junjun Li[1], Miaohui Li[1], Qiang Li[1], Shanshan Li[1], Shi Li[1], Yadong Li[1], Yingying Li[1], Lizhen Liang[1], Yanchuan Liao[1], Shiyao Lin[1], Bili Ling[1], Changle Liu[1], Haiqing Liu[1], Huajun Liu[1], Liang Liu[1], Shaocheng Liu[1], Sheng Liu[1], Xiaogang Liu[1], Xiaoju Liu[1], Yong Liu[1], Zhihong Liu[1], Zhimin Liu[1], Zixi Liu[1], Feng Long[1], Jianhua Lu[1], Zhengping Luo[1], Bo Lyu[1], Dengkui Ma[1], Lin Ma[1], Huafeng Mao[1], Wendong Ma[1], Songtao Mao[1], Yuzhou Mao[1], Tingfeng Ming[1], Chao Mo[1], Qicai Ni[1], Minzhong Qi[1], Chao Pan[1], Chengkang Pan[1], Shengmin Pan[1], Jing Qian[1], Jinping Qian[1], Li Qian[1], Yanda Qian[1], Chengming Qin[1], Lilong Qiu[1], Qilong Ren[1], Zhibin Ren[1], Junsong Shen[1], Linhai Sheng[1], Peng Sheng[1], Zhicai Sheng[1], Nan Shi[1], Shihua Song[1], Pengjun Sun[1], Xiaoyang Sun[1], Youwen Sun[1], Jie Tang[1], Ling Tao[1], Ang Ti[1], Erhui Wang[1], Feng Wang[1], Fudi Wang[1], Houyin Wang[1], Huazhong Wang[1], Huihui Wang[1], Huiqian Wang[1], Jian Wang[1], Lei Wang[1], Liang Wang[1], Linsen Wang[1], Mao Wang[1], Ping Wang[1], Shengming Wang[1], Wanjing Wang[1], Xiaojie Wang[1], Xiaoming Wang[1], Yating Wang[1], Yiyun Wang[1], Yong Wang[1], Yumin Wang[1], Jianglong Wei[1], Jing Wei[1], Xuechao Wei[1], Bin Wu[1], Dajun Wu[1], Hao Wu[1], Jinhua Wu[1], Xiangming Wu[1], Yibing Wu[1], Zhenwei Wu[1], Zege Wu[1], Weibin Xi[1], Genhai Xiao[1], Tianyang Xia[1], Yezheng Xiao[1], Hunyi Xie[1], Yahong Xie[1], Yuanlai Xie[1], Chandong Xu[1], Jichan Xu[1], Li Xu[1], Liqing Xu[1], Tiejun Xu[1], Yongjian Xu[1], Ning Yan[1], Fei Yang[1], Jianhua Yang[1], Lei Yang[1], Qingxi Yang[1], Yao Yang[1], Yong Yang[1], Zhongshi Yang[1], Min Yu[1], Yaowei Yu[1], Qiping Yuan[1], Shuai Yuan[1], Qing Zang[1], Long Zeng[1], Jizong Zhang[1], Kai Zhang[1], Liyuan Zhang[1], Ling Zhang[1], Ruirui Zhang[1], Shoubiao Zhang[1], Tao Zhang[1], Wei Zhang[1], Xinjun Zhang[1], Yang Zhang[1], Zuchao Zhang[1], Hailin Zhao[1], Jinlong Zhao[1], Fubin Zheng[1], Yuanyang Zheng[1], Guoqiang Zhong[1], Ruijie Zhou[1], Haishan Zhou[1], Yue Zhou[1], Dahuan Zhu[1], Haisheng Zhu[1], Ping Zhu[1], Zeying Zhu[1], Huidong Zhuang[1], Zibo Zhou[1], Zhiyong Zhou[1], Zhiwei Zhou[1], Guizhong Zuo[1].

International and Domestic Collaborators:

Tao Lan[2], Adi Liu[2], Wandong Liu[2], Hong Qin[2,16], Shaojie Wang[2], Minyou Ye[2], Yi Yu[2], Ping Zhu[2], Wei Chen[3], Guangjiu Lei[3], Lin Nie[3], Xianming Song[3], Min Xu[3], Yuhong Xu[3], Huang Yuan[3], Nanhua Yao[3], Zhe Gao[4], Yuhe Li[4], Zhongjing Chen[5], Tieshuan Fan[5], Xingyu Peng[5], Liu Chen[6,21], Zhiwei Ma[6], Zhiyong Qiu[6], Zengmao Sheng[6], Yong Xiao[6], Xiaogang Wang[7], Zhongyong Chen[8], Yonghua Ding[8], Xiwei Hu[8], Zijiang Wang[8], Ge Zhuang[8], Daming Liu[9], Jiarong Luo[9], Fangchuan Zhong[9], Hongbin Ding[10], Dezhen Wang[10], Zhengxiong Wang[10], Chenggang Jin[11], Xuemei Wu[11], Xiaofei Yang[11], Jianhua Zhang[12], Qingyuan Hu[12], Xi Yuan[12], Changqi Chen[13], Shuyi Gan[13], Xudi Wang[13], Congzhong Wu[13], Chongwei Zhang[13], Ting Zhang[13], Wu Zhu[13], Erhua Kong[14], Kaisong Wang[14], Chuanli Wang[14], Hongtao Yang[14], Lixiang Zhang[14], Paul Anderson[15], Gheni Abla[15], Vincent Chan[15], John L. Doane[15], Andrea Garofalo[15], Punit Gohil[15], Houyang Guo[15], David Hill[15], Chris Holcomb[15], Chung Lih Hsieh[15], Ruey Hong[15], David Humphreys[15], Alan Walter Hyatt[15], Gary Jackson[15], Egemen Kolemen[15],

Matthew Lanctot[15], Lang Lao[15], James Leuer[15], John Lohr[15], Mohamad Ali Mahdavi[15], Robert Olstad[15], Ben Penaflor[15], Ron Prater[15], David Piglowski[15], Michael Schaffe[15], Eugenio Schuster[15], Tim Scoville[15], Wayne Solomon[15], Gary Staebler[15], Mickey Wade[15], Mike Walker[15], Anders Welander[15], Manfred Bitter[16], Robert Budny[16], Robert A. Ellis[16], Guoyong Fu[16], Nat Fisch[16], Rich Hawryluk[16], Kenneth W. Hill[16], Joel Hosea[16], Michael A. Jaworski[16], Egemen Kolemen[16], Dennis Mansfield[16], Dana M. Mastrovito[16], Jonathan Menard[16], Dennis Mueller[16], Novmir Pablant[16], Yang Ren[16], Lane Roquemore[16], Filippo Scotti[16], Gary Taylor[16], Kevin Tritz[16], Randy Wilson[16], Michael Zarnstorff[16], Leonid E. Zakharov[16], Seung Gyou Baek[17], Beck Bill[17], Paul T. Bonoli[17], Robert Granetz[17], Yijun Lin[17], Ron Parker[17], Shunichi Shiraiwa[17], Josh Stillerman[17], Greg Wallace[17], Stephen Wukitch[17], Lihua Zhou[17], He Huang[18], Kenneth Gentle[18], Ken Liao[18], Perry Philippe[18], William L. Rowan[18], Linjin Zheng[18], Patrick H. Diamond[19], George R.Tynan[19], Nicolas Fedorczak[19], Peter Manz[19], Lei Zhao[19], David Brower[20], Weixing Ding[20], William W. Heidbrink[21], Yubao Zhu[21], Calvin W. Domier[22], Neville C. Luhmann[22], Xueqiao Xu[23], Eric Wang[23], Max E. Fenstermarcher[23], Donald L. Hillis[24], Rajesh Maingi[24], Steve Meitner[24], Igor V. Vinyar[25], Vladimir Davydenko[26], Igor Shikhovtsev[26], Naoko Ashikawa[27], Kasahara Hiroshi[27], Katsumi Ida[27], Shinichiro Kado[27], Tomita Kawamura[27], Saito Kenji[27], Ryuhei Kumazawa[27], Ogawa Kunihiro[27], Isobe Mitsutaka[27], Shigeru Morita[27], Haruhisa Nakano[27], Satoshi Ohdachi[27], Masaki Osakabe[27], Mizuki Sakamoto[27], Yasuhiko Takeiri[27], Kazuo Toi[27], Katsuyoshi Tsumori[27], Nobuta Yuji[27], Masaya Hanada[28], Mitsuru Kikuchi[28], Atsushi Kojima[28], Kazuhiro Watanabe[28], Jean-Francois Artaud[29], Vincent Basiuk[29], F. Bouquey[29], B. Bremond[29], Gilles Coledani[27], Laurent Colas[29], Joan Decker[29], D. Douai[29], Annika Ekedahl[29], Christel Fenzi[29], Eric Gauthier[29], Gerardo Giruzzi[29], Marc Goniche[29], Dominique Guilhem[29], Walid Helou[29], Julien Hillairet[29], Tuong Hoang[29], Philippe Huynh[29], Frederic Imbeaux[29], Xavier Litaudon[29], Roland Magne[29], Yves Peysson[29], K. Vueillie[29], Xiaolan Zou[29], Alberto Loarte[30], Franz Braun[31], R. Bilato[31], Volodymyr Bobkov[31], J.M. Noterdaeme[31], Qingquan Yu[31], Yunfeng Liang[32], Jonny Pearson[32], Michael Rack[32], John Fessey[33], Yueqiang Liu[33], Charles Monroe[33], Stefan Schmuck[33], Paul Trimble[33], Tom Todd[33], Cheonho Bae[34], Jun-Gyo Bak[34], Suk-Ho Hong[34], Sangong Lee[34], Bae Young Soon[34], Oh Byung Hoon[35], Chang Doo Hee[35], Lee Kwang Won[35], Luca Amicucci[36], Giuseppe Calabro[36], Silvio Ceccuzzi[36], Roberto Cesario[36], Flavio Crisanti[36], Edmondo Giovannozzi[36], Giuseppe Ramogida[36], Gianmaria. De Tommasi[36], Angelo Antonio Tuccillo[36], Bruno Viola[36], Raffaele Albanese[37], Roberto Ambrosino[37], Lucio Barbato[37], Stefano Mastrostefano[37], Alfredo Pironti[37],Vincenzo Pericoli Ridolfini[37], Rory Scannell[37], Fabio Villone[37], Volker Naulin[38], Anders H. Nielsen[38], Roman Zagorsky[39], Sandor Zoletnik[40], Chijin Xiao[4]1, B.Madsen[42] and M. Salewski[42]

[1]Institute of Plasma Physics, Chinese Academy of Sciences, Hefei 230031, China
[2]University of Science and Technology of China, Hefei 230026, China
[3]Southwestern Institute of Physics, Chengdu 610041, China
[4]Tsinghua University, Beijing, China
[5]Peking University, Beijing, China
[6]Zejiang University, Hangzhou, China
[7]Harbin Institute of Technology, Harbin 150001, China
[8]Huazhong University of Science and Technology, Wuhan, China
[9]Donghua University, Shanghai, China
[10]Dalian University of Technology, Dalian 116024, China
[11]Soochow University, Shuzhou, China
[12]China Academy of Engineering Physics, Mianyang 621900, China
[13]Hefei University of Technology, Hefei 230009, China
[14]Anhui University of Science and Technology, Huainan 232001, China

[15]General Atomic, San Diego, CA 92186-5608, USA
[16]Princeton Plasma Physics Laboratory, PO Box 451, Princeton, NJ 08543, USA
[17]Massachusetts Institute of Technology, Plasma Science and Fusion Center, Cambridge, MA 02139, USA
[18]Fusion Research Center, University of Texas at Austin, Austin, TX 78712, USA
[19]University of California, San Diego, CA 92093, USA
[20]University of California Los Angeles, Los Angeles, CA 90095, USA
[21]University of California at Irvine, Irvine, CA 92697, USA
[22]University of California at Davis, Davis, CA 95616, USA
[23]Lawrence Livermore National Laboratory (LLNL), Livermore, CA 94551, USA
[24]Oak Ridge National Laboratory, Oak Ridge, TN 37831-6169, USA
[25]PELIN, LLC, 27A, Gzhatskaya, Saint Petersburg 195220, Russia
[26]Budker Institute of Nuclear Physics, Novosibirsk 630090, Russia
[27]National Institute for Fusion Sciences, Toki 509-5292, Japan
[28]Japan Atomic Energy Research Institute, Naka-machi, Naka-gun, Ibaraki-ken 311-0193, Japan
[29] CEA Cadarache, IRFM, F-13108 Saint Paul-lez-Durance, France
[30]ITER Organization, Route de Vinon sur Verdon, 13115 St Paul Lez Durance, France
[31]Max-Planck Institute for Plasma Physics, D-85748, Garching, Germany
[32]Association EURATOM-FZJ, D-52425 Jülich, Germany
[33]Euratom/CCFE Fusion Association, Culham Science Centre, Abingdon, Oxon. OX14 3DB, UK
[34]National Fusion Research Institute, Yuseong-Gu, Daejeon, 305-806, Korea
[35]Korea Atomic Energy Research Institute,Yuseong-Gu, Daejeon, 305-353,Korea
[36]ENEA Unità Tecnica Fusione, C.R. Frascati, Via E. Fermi 45, 00044 Frascati, Roma, Italy
[37]CREATE, Università di Napoli Federico II, Università di Cassino and Università di Napoli Parthenope, Via Claudio 19, 80125 Napoli, Italy
[38]Association Euratom-Risø DTU, Roskilde, Denmark
[39]Institute of Plasma Physics and Laser Microfusion, Warsaw, Poland
[40]Association EURATOM - KFKI RMKI, P.O. Box 49, H-1525 Budapest, Hungary
[41]University of Saskatchewan, Saskatchewan, S7N 5E5, Canada
[42]Department of Physics, Technical University of Denmark, Kgs. Lyngby, Denmark

REFERENCES

[1] Wan B.N. *et al* 2019 *Nucl. Fusion* **59** 112003

[2] Wan Y. *et al* 2017 *Nucl. Fusion* **57** 102009

[3] Zhuang G. *et al* 2019 *Nucl. Fusion* **59** 112010

[4] Gong X. *et al* EAST steady-state long pulse H-mode with core-edge integration for CFETR, *submitted to Nucl. Fusion*

[5] Gong X. *et al* 2019 *Nucl. Fusion* **59** 086030

[6] Sauter O. *et al* 1999 *Phys. Plasmas* **6** 2834

[7] Qian J.P. 2021 *Phys. Plasmas* **28** 042506

[8] Kishimoto H. *et al* 2005 *Nucl. Fusion* **45** 986

[9] Qian J.P *et al* 2017 *Nucl. Fusion* **57** 084001

[10] Wan B.N. 2020 *Chin. Phys. Lett.* **37** 045202

[11] Huang J. *et al* 2020 *Nucl. Fusion* **60** 016002

[12] Huang J. *et al* 2020 *Plasma Phys. Control. Fusion* **62** 014019

[13] Madsen B. *et al* 2020 *Plasma Phys. Control. Fusion* ***62*** 115019

[14] Salewski M. *et al* 2016 *Nucl. Fusion* **56** 106024

[15] Salewski M. *et al* 2018 *Nucl. Fusion* **58** 036017

[16] Xu G.S. 2019 *Phys. Rev. Lett.* **122** 255001

[17] Xu G.S *et al* 2020 *Nucl. Fusion* **60** 086001

[18] Yang Q.Q. *et al* 2020 *Nucl. Fusion* **60** 076012

[19] Kamada Y. *et al* 2000 *Plasma Phys. Control. Fusion* **42** A247

[20] Aiba N. and Oyama N. 2012 *Nucl. Fusion* **52** 114002;

[21] Snyder P. B. *et al* 2002 *Phys. Plasmas* **9** 2037

[22] Li K. D. *et al* 2020 *Plasma Phys. Control. Fusion* **62** 095025

[23] Pitts R. A. *et al* 2019 *Nucl. Mater. Energy* **20** 100696

[24] Wang L. *et al* Achievements of Actively Controlled Divertor Detachment Compatible with Sustained High Cnfinement Core in DIII-D and EAST, *submitted to Nucl. Fusion*

[25] Yuan Q.P. *et al* 2020 *Fusion Eng. Des.* **154** 111557

[26] Eldon D. *et al* 2021 *Nucl. Mater. Energy* **27** 100963

[27] Chen M.W. *et al* 2020 *Nucl. Fusion* **60** 076009

[28] Wang L. *et al* 2021 *Nature Commun.* **12** 1365

[29] Tabares, F.L. *et al* 2016 *Nucl. Fusion* **56** 127002

[30] Hu J.S. *et al* 2016 *Nucl. Fusion* **56** 046011

[31] Zuo G.Z. *et al* 2019 *Nucl. Fusion* **59** 016009

[32] Zuo G.Z. *et al* 2018 *Fusion Eng. Des.* **137** 420

[33] Zuo G.Z. *et al* 2017 *Rev. Sci. Instrum* **88** 123506

[34] Li C.L. *et al* 2021 *Plasma Phys. Control. Fusion* **63** 015001

[35] Zuo G.Z. *et al* 2020 *Phys. Plasmas* **27** 052506

[36] Xu G.S. *et al* Sustained Edge-Localized-Modes suppression and radiative divertor with an impurity-driven instability in tokamak plasmas, *submitted to Nucl. Fusion*

[37] Wu K. *et al* 2021 *Plasma Phys. Control. Fusio*n **63** 105004

[38] Nagy A. *et al* 2018 *Rev. Sci. Instrum* **89** 10K121

[39] Sun Z. *et al* 2021 *Nucl. Fusion* **61** 014002

[40] Sun Z. *et al* 2021 *Phys. Plasmas* **28**, 082512

[41] Maingi R. *et al* 2020 *J. Fusion Energy* **39** 429-435

[42] Sun Z. *et al* 2021 *Nucl. Fusion* **61**, 066022

[43] Bernert M. *et al* 2021 *Nucl. Fusion* **61** 024001

[44] Osborne T. H. *et al* 2015 *Nucl. Fusion* **55**, 063018

[45] Gilson E. P. *et al* 2021 *Nucl Mater Energy* **28**

[46] Wang H.Q. *et al* 2014 *Phys. Rev. Lett.* **112** 185004

[47] Wang H.Q. *et al* 2014 *Phys. Plasmas* **21** 092551

[48] Chen R. *et al* 2018 *Nucl. Fusion* **58** 112004

[49] Xia T.Y and Xu X.Q 2015 *Nucl. Fusion* **55** 113030

[50] Xia T. Y. *et al* 2019 *Nucl Fusion* **59** 076043

[51] Xi P. W. *et al* 2014 *Phys. Rev. Lett.* **112** 085001

[52] Xia T. *et al* The simulation of ELMs mitigation by pedestal coherent mode in EAST using BOUT++, *submitted to Nucl. Fusion*

[53] Sun Y. *et al* 2021 *Nucl. Fusion* in press https://doi.org/10.1088/1741-4326/ac1a1d

[54] Budny R. V. *et al* 2008 *Nucl. Fusion* **48**, 075005

[55] Sun Y. *et al* 2016 *Phys. Rev. Lett*. **117** 115001

[56] Sun Y. *et al* 2017 *Nucl. Fusion* **57** 036007

[57] Liu Y.Q. *et al* 2010 *Phys. Plasmas* **17** 122502

[58] Loarte A. *et al* Integrated ELM and divertor flux control using RMPs with low input torque in EAST in support of the ITER research plan Preprint: 2020 IAEA Fusion Energy Conference, Nice [EX/4-4Ra]

[59] Jia M. *et al* 2021 *Nucl. Fusion* in press https://doi.org/10.1088/1741-4326/ac21f9

[60] Jia M. *et al* 2016 *Plasma Phys. and Control. Fusion* **58** 055010

[61] Jia M. *et al* 2018 *Nucl Fusion* **58** 046015

[62] Zhang B. *et al* 2020 *Nucl. Fusion* **60** 092001

[63] Zhang B. *et al* H-mode Operation in He Plasmas with pure RF-Heating and ITER-like Tungsten Divertor on EAST, Preprint: 2020 IAEA Fusion Energy Conference, Nice [P2-917]

[64] Ryter F. *et al* 2009 *Nucl. Fusion* **49** 062003

[65] Ding R. *et al* Plasma-wall interactions during the helium plasma operation in EAST with a tungsten divertor, Preprint: 2020 IAEA Fusion Energy Conference, Nice [P2-1068]

[66] Wu K. *et al* 2018 *Nucl. Fusion* **58** 056019

[67] Ding F. *et al* 2019 *Tungsten* **1** 122

[68] Abrams T. 2019 *Phys. Plasmas* **26** 062504

[69] Harder N.D. *et al* 2016 *Nucl. Fusion* **56** 026014

[70] Ding R. *et al* 2015 *Nucl. Fusion* **55** 023013

[71] Möller S. *et al* 2020 *Nucl. Mater. Energy* **25** 100805

[72] Li L. *et al* 2021 *Plasma Science Tech.* **23** 095601